

Bioinspired adaptive visual servoing control for quadrotors

Hazelaar, S.T.; Wang, C.; de Wagter, C.; Muijres, Florian T.; de Croon, G.C.H.E.; Yedutenko, M.

DOI

[10.1088/1748-3190/adcdde](https://doi.org/10.1088/1748-3190/adcdde)

Publication date

2025

Document Version

Final published version

Published in

Bioinspiration & Biomimetics: learning from nature

Citation (APA)

Hazelaar, S. T., Wang, C., de Wagter, C., Muijres, F. T., de Croon, G. C. H. E., & Yedutenko, M. (2025). Bioinspired adaptive visual servoing control for quadrotors. *Bioinspiration & Biomimetics: learning from nature*, 20(3), Article 036014. <https://doi.org/10.1088/1748-3190/adcdde>

Important note

To cite this publication, please use the final published version (if applicable). Please check the document version above.

Copyright

Other than for strictly personal use, it is not permitted to download, forward or distribute the text or part of it, without the consent of the author(s) and/or copyright holder(s), unless the work is under an open content license such as Creative Commons.

Takedown policy

Please contact us and provide details if you believe this document breaches copyrights. We will remove access to the work immediately and investigate your claim.

PAPER • OPEN ACCESS

Bioinspired adaptive visual servoing control for quadrotors

To cite this article: Sander T Hazelaar *et al* 2025 *Bioinspir. Biomim.* **20** 036014

View the [article online](#) for updates and enhancements.

You may also like

- [Biomimetic seal whisker sensors for high-sensitivity wake detection and localization](#)
Biao Geng, Qian Xue, Zhiheng Xu et al.
- [Ethics of biohybrid robotics and invertebrate research: biohybrid robotic jellyfish as a case study](#)
Nicole W Xu, Olga Lenczewska, Sarah E Wieten et al.
- [Aerodynamic effect of stroke amplitude on hovering performance of a three-dimensional tandem flapping wing](#)
Shubham Tiwari, DG Thakur and Sunil Chandel

Bioinspiration & Biomimetics



PAPER

Bioinspired adaptive visual servoing control for quadrotors

OPEN ACCESS

RECEIVED

31 December 2024

REVISED

25 March 2025

ACCEPTED FOR PUBLICATION

16 April 2025

PUBLISHED

9 May 2025

Original Content from this work may be used under the terms of the [Creative Commons Attribution 4.0 licence](https://creativecommons.org/licenses/by/4.0/).

Any further distribution of this work must maintain attribution to the author(s) and the title of the work, journal citation and DOI.



Sander T Hazelaar^{1,3} , Chenyao Wang^{2,3} , Christophe de Wagter¹ , Florian T Muijres² , Guido C H E de Croon¹  and Matthew Yedutenko^{1,*} 

¹ Micro Air Laboratory, Faculty of Aerospace Engineering, Delft University of Technology, Delft, The Netherlands

² Experimental Zoology Group, Wageningen University, Wageningen, The Netherlands

³ Contributed equally to this work.

* Author to whom any correspondence should be addressed.

E-mail: m.yedutenko@tudelft.nl

Keywords: visual servoing, optical flow, bioinspired robotics, autonomous navigation, landing, insect landings

Abstract

Since every flight ends in a landing and every landing is a potential crash, deceleration during landing is one of the most critical flying maneuvers. Here we implement a recently-discovered insect visual-guided landing strategy in which the divergence of optical flow is regulated in a step-wise fashion onboard a quadrotor for the task of visual servoing. This approach was shown to be a powerful tool for understanding challenges encountered by visually-guided flying systems. We found that landing on a relatively small target requires mitigation of the noise with adaptive low-pass filtering, while compensation for the delays introduced by this filter requires open-loop forward accelerations to switch from divergence setpoint. Both implemented solutions are consistent with insect physiological properties. Our study evaluates the challenges of visual-based navigation for flying insects. It highlights the benefits and feasibility of the switching divergence strategy that allows for faster and safer landings in the context of robotics.

1. Introduction

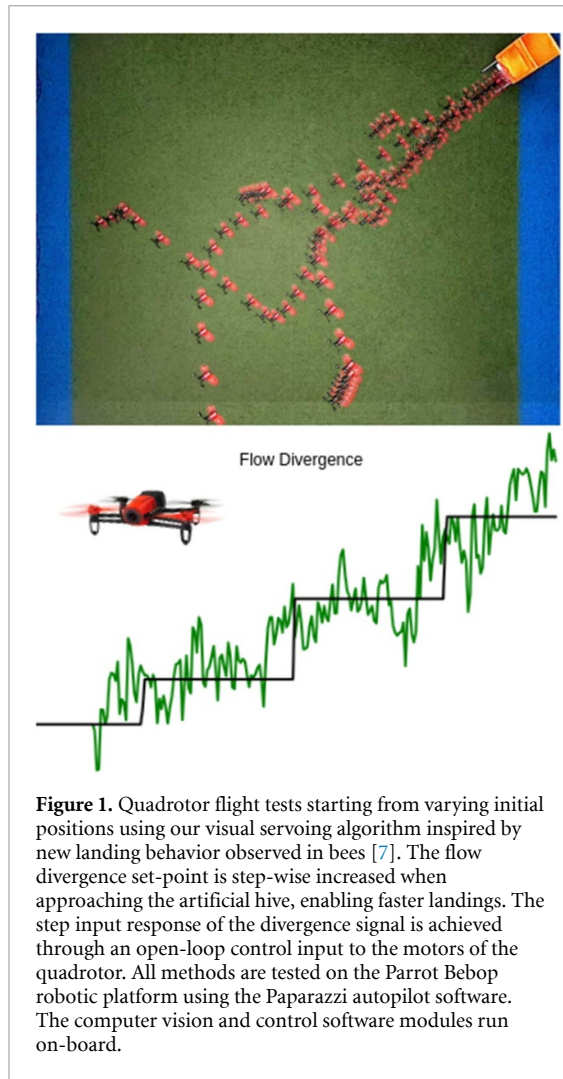
Since every flight ends in a landing and every landing is a potential crash, deceleration during landing is one of the most critical flying maneuvers. Insects, renowned as masters of flight, capable of performing more than 1000 landings per hour [1], rely heavily on vision to control their deceleration [2–10]. Studies in various species of insects [3, 4] reveal that insects begin to decelerate towards their target as soon as visual control becomes feasible—when the change in the visual size of the target exceeds the spatial resolution limit of the insect.

How exactly do insects regulate their deceleration? Upon analysis of honeybee mean landing traces averaged across multiple repeats in windless conditions, Baird *et al* [3] proposed a highly influential theory that insects land by keeping the expansion rate of the target's image (also known as the divergence of optical flow) constant. Since this divergence describes the ratio between approaching speed and distance to the target, by keeping it constant, a honeybee gradually decreases its velocity upon a decrease in

distance. Although some studies confirmed this theory for other species, such as bumblebees [5, 10], experiments with headwind [10] and fruit flies [4] suggested that divergence does not remain constant during landing.

Goyal *et al* [5–7] provided key insights by analyzing individual landing traces of honeybees and bumblebees, rather than relying on mean landing traces. Their findings revealed that both species regulate divergence during landing in a stepwise fashion (figure 1). Notably, this effect disappears when mean landing traces, as analyzed in [3], are used. Although analyzing individual landing traces helps to gain insights, the proposed landing strategy merely describes the observed trajectory. It does not necessarily function as a control law, which is shaped by real-world constraints. To fully understand the challenges insects face during landing, it is essential to implement an insect navigation pipeline that accounts for real-world limitations.

For such a task, robots serve as excellent model 'organisms', because they enable real-world testing of concepts derived from animal observations while



ensuring interpretability and full control over the system [11, 12], which is often a problem in the fields of system and computational biology [13]. Numerous studies have gained significant insights into the nature of the tasks faced by flying insects and their corresponding solutions by studying flapping wing and quadrotor drones [11, 14–25]. Specifically, for the case of landing strategies, the naive robotic implementation (i.e. with constant control gain) of constant divergence deceleration revealed that sensing and actuation delays led to instabilities in the control loop close to the landing surface [26, 27]. These instabilities led to oscillations in divergence and the agent’s position and resulted in a crash [26, 27]. Therefore, to ensure stability, the flying agent needs to regulate its control gain upon approach [26, 27].

Here, we implemented the ‘switching’ divergence strategy discovered by Goyal *et al* [5–7] to mimic bumblebees landing into the nest by landing the drone into the box ($0.6 \times 0.6 \times 0.6 \text{ m}^3$) through a frontal window (figures 1, 13). It is important, that in contrast to many other studies on visual-guided drone landing [21, 25, 27–34], where landing was

done on large flat surfaces, the landing surface in our experiments was relatively small. This required much higher control precision. In the robotics field, this type of task is called visual servoing and considered to be much more challenging than simply landing [35–37]. Yet, this is precisely the type of landing insects do. Therefore, this approach brought us closer to the real-world challenges faced by insects.

We encountered three major algorithmic (i.e. relevant for any flying system) challenges in implementing a ‘switching’ divergence strategy for visual servoing. First, we observed a dramatic increase in noise in the divergence signal upon increase in distance to the target, originating from the increase in noise in the estimate of the target visual size (figure 8). Secondly, we found that proportional-integral-derivative (PID) control of the divergence switch led to oscillations in the divergence signal upon a set-point switch, slowing down system response. Thirdly, we encountered the previously described issue of oscillations near the target surface. We addressed these problems by using solutions consistent with the known capabilities of insect control and visual systems: adaptive temporal filtering to combat noise [38], open-loop forward accelerations to counteract delays and oscillations upon a set-point switch [9], and a decrease in control gain upon approaching the target to prevent oscillations near the surface [39].

To summarize, our study shed light on the challenges insects and other flying agents encounter during visually-guided landings and demonstrated how these challenges can be addressed with bioinspired solutions.

2. Framework: visual-based landings of a quadrotor

To investigate visual-based servoing, we focused on the task of landing. Our experiments, conducted indoors with a quadrotor (Parrot Bebop), mimicked the landing of a honeybee in its hive (figure 2). For this, we placed an artificial ‘hive’ in the testing area. The ‘hive’ consisted of a box with a front window, with both its interior and exterior painted orange to improve detectability (figure 2).

The quadrotor was equipped with the Paparazzi autopilot software (figure 3) and a standard set of sensors, including a wide-angle front camera and an IMU. In addition, the position and orientation of the drone were continuously tracked using a motion capture system (OptiTrack). OptiTrack transmitted signals in real-time via Ethernet to a computer ground station, which was connected to the quadrotor via WiFi. OptiTrack’s position measurements were used only to evaluate flight performance. Attitude measurements were used to improve the IMU readings with a Kalman filter (see below). Although attitude

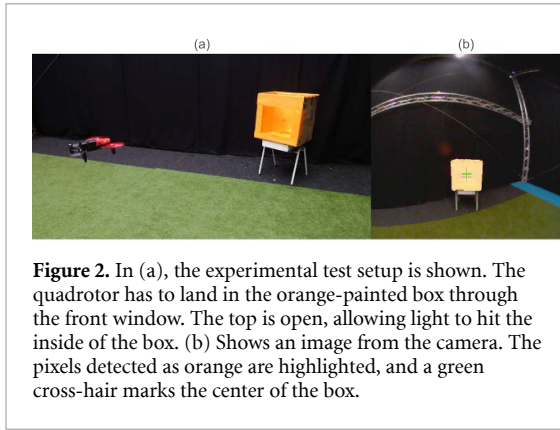


Figure 2. In (a), the experimental test setup is shown. The quadrotor has to land in the orange-painted box through the front window. The top is open, allowing light to hit the inside of the box. (b) Shows an image from the camera. The pixels detected as orange are highlighted, and a green cross-hair marks the center of the box.

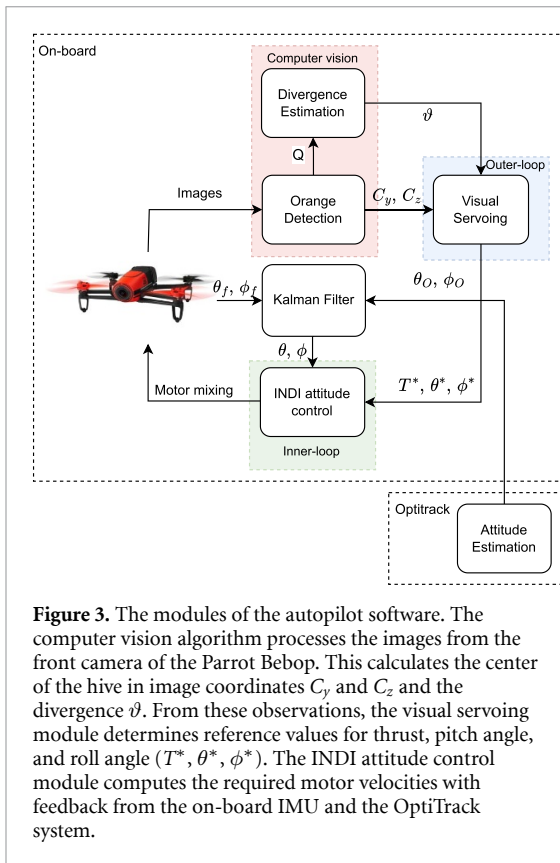


Figure 3. The modules of the autopilot software. The computer vision algorithm processes the images from the front camera of the Parrot Bebop. This calculates the center of the hive in image coordinates C_y and C_z and the divergence ϑ . From these observations, the visual servoing module determines reference values for thrust, pitch angle, and roll angle (T^* , θ^* , ϕ^*). The INDI attitude control module computes the required motor velocities with feedback from the on-board IMU and the OptiTrack system.

measurements streamlined testing, they were not required for the visual servoing controller.

The images were collected with a spatial resolution of 400×400 pixels, at an average frame rate of 11.4 Hz, and fed to the onboard computer vision module. There, the orange box was detected and two subsequent images were compared to estimate optical flow divergence (see below for the details), which was fed to the control module. The control module consisted of outer and inner loops (see below for details). The outer loop controlled the position via PID control, while the inner loop controlled the drone attitude.

2.1. Visual servoing controller

Below, we discuss the functioning of the visual servoing controller.

Consider the situation shown in figure 4. The position of the quadrotor ξ is given in the inertial reference frame (X_I, Y_I, Z_I) , which has its origin fixed at the center of the ‘hive’. The attitude (ϕ, θ, ψ) of the quadrotor defines the rotation of the body frame (X_b, Y_b, Z_b) with respect to the inertial frame.

The quadrotor uses a single camera that points forward in the X_b direction, which is assumed to be located at the center of gravity of the MAV. Figure 4 shows the plane of the image with the coordinates of the center of the hive defined as C_y and C_z , and the optical flow divergence ϑ that occurs when approaching the hive, given by:

$$\vartheta = -\frac{v}{d} \quad (1)$$

where d is the Euclidean distance to the ‘hive’, and v is its time derivative. Note that during the landing v is negative. Therefore, the minus sign is included to make the divergence positive when approaching the hive.

With reference frames being defined, we can examine the quadrotor’s control system. A quadrotor is an under-actuated system, which can be viewed as two connected subsystems. We can design a control law with inner and outer loops. The outer loop controls the position ξ of the quadrotor by rotating the thrust vector. The inner loop handles the attitude through the angular velocity of the four propellers.

For the outer loop controller, we examine the position dynamics of a quadrotor, keeping the yaw angle ψ fixed:

$$\ddot{\xi} = \begin{bmatrix} 0 \\ 0 \\ g \end{bmatrix} + \frac{1}{m} \begin{bmatrix} \cos \phi \sin \theta \\ -\sin \phi \\ \cos \phi \cos \theta \end{bmatrix} T + \frac{1}{m} \mathbf{F}(\dot{\xi}, w) \quad (2)$$

where g is the gravitational acceleration, m is the mass, T is the total thrust force, and F is the aerodynamic force, which is a function of velocity and wind w . The following control law can be used to find the desired values μ for $\ddot{\xi}$ with feedback from the camera:

$$\mu_x = k_{p_x} * (\vartheta^* - \vartheta) + k_{i_x} * \int (\vartheta^* - \vartheta) \quad (3)$$

$$\mu_y = k_{p_y} * C_y + k_{d_y} * \frac{d}{dt} (C_y) + k_{i_y} * \int (C_y) \quad (4)$$

$$\mu_z = k_{p_z} * C_z + k_{d_z} * \frac{d}{dt} (C_z) + k_{i_z} * \int (C_z) + g \quad (5)$$

where k_p , k_i , k_d are the proportional, integral, and derivative gains, ϑ^* is the divergence set-point, and the reference values for the centroid are set to zero. In this way, the centroid of the hive in terms of C_y and C_z is used to center the quadrotor on the ‘hive’, while the divergence ϑ regulates the forward acceleration.

The reference values of attitude θ^* , ϕ^* and thrust T^* can be determined with equation (2):

$$T^* = \sqrt{\mu_x^2 + \mu_y^2 + \mu_z^2} * m \quad (6)$$

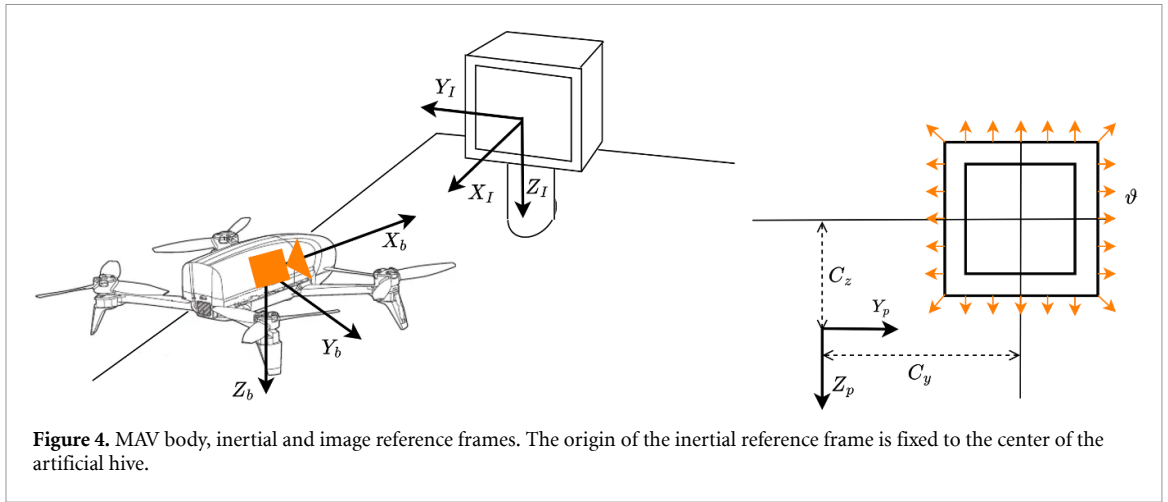


Figure 4. MAV body, inertial and image reference frames. The origin of the inertial reference frame is fixed to the center of the artificial hive.

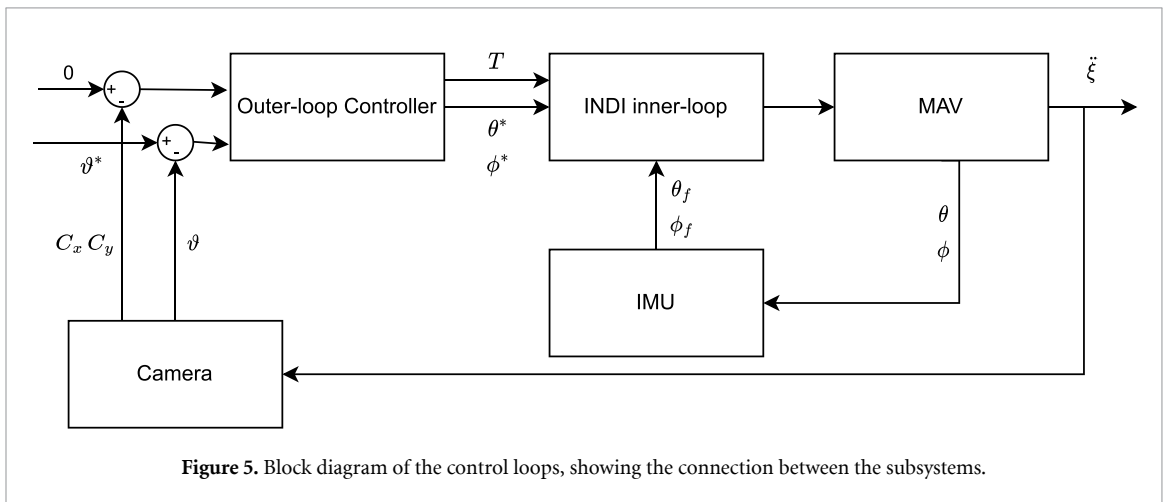


Figure 5. Block diagram of the control loops, showing the connection between the subsystems.

$$\theta^* = \arctan \left(\frac{\mu_x}{\mu_z} \right) \quad (7)$$

$$\phi^* = \arcsin \left(\frac{m\mu_y}{T} \right). \quad (8)$$

The set-points for attitude and thrust are fed into an inner control loop, which calculates the motor velocities of the four propellers through incremental non-linear dynamic inversion (INDI). Here, we used an implementation developed in [40].

The complete control system with inner and outer loops is summarized in figure 5. This controller cannot be implemented directly since the non-linear system dynamics require online adaptation of all controller gains in equation (3) [26]. These gains must be proportional to the Euclidean distance to the hive d . The proposed solution to this problem is described in subsection 4.3.

As the quadrotor nears the hive during landing, it gets so close that visual cues become undetectable, causing a loss of control feedback. To land, a pre-programmed landing procedure is initiated at a specific visual size of the hive. This maneuver takes 1 s and starts with a forward acceleration. This is followed by a descent, after which the motors are shut down.

3. Analysis of benefits of step-wise divergence regulation

When divergence is kept constant, the distance to the target exponentially decays over time, as described by the equation:

$$d = d_0 e^{-\vartheta^* t} \quad (9)$$

which is plotted in figure 6 (red). The switching strategy is a series of such exponential decays (figure 6, green). The same exponential decay also describes the change in speed over time (figure 6, dotted lines).

One trivial benefit of the switching strategy is that it allows for a faster landing. Landing with constant divergence leads to deceleration (figure 6(A), red dotted line). An increase in divergence set-point leads to an increase in speed (green dotted line). By definition, an increase in speed will make the landing faster (figure 6(A)). However, the same faster landing can be achieved with simply a higher initial divergence set-point. Therefore, simply faster landing upon a switch to a higher divergence emphasizes not the

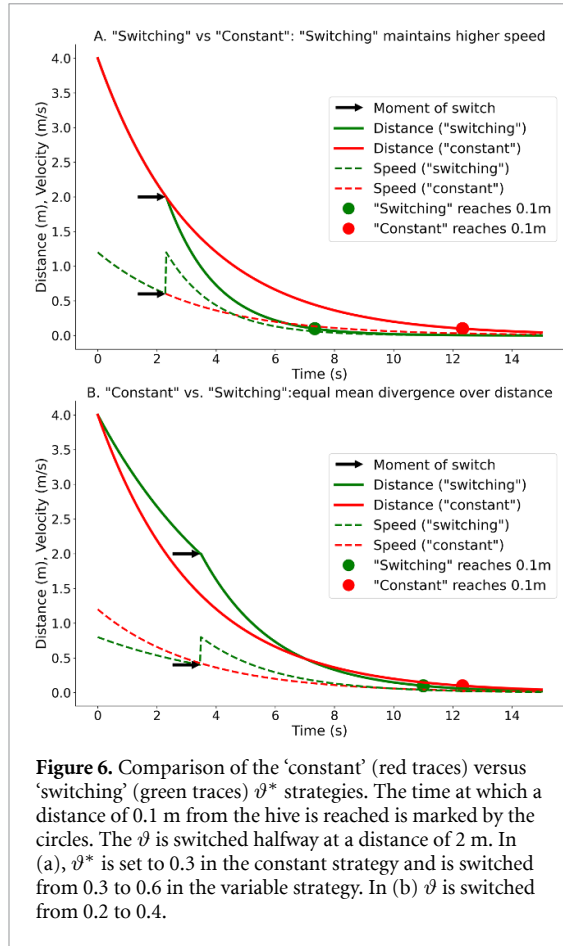


Figure 6. Comparison of the ‘constant’ (red traces) versus ‘switching’ (green traces) ϑ^* strategies. The time at which a distance of 0.1 m from the hive is reached is marked by the circles. The ϑ is switched halfway at a distance of 2 m. In (a), ϑ^* is set to 0.3 in the constant strategy and is switched from 0.3 to 0.6 in the variable strategy. In (b) ϑ is switched from 0.2 to 0.4.

benefit of switching, but the benefit of higher divergence (though note that real-world systems have limited maximal speed and hence limited maximal divergence for a given distance).

To isolate the effect of switching from the effect of simply higher divergence, we analytically compared the performance of switching and constant divergence strategies while keeping the divergence averaged over the flown distance equal. Our analysis, detailed in appendix A, shows that given sufficient flying distance, the switching strategy would lead to a shorter landing time than the constant divergence strategy (figure 6(B)). Effectively, the switching strategy allows the drone to land faster using a smaller maximal speed, which makes flight safer in cluttered environments (figure 6, dotted line).

4. Optical flow based navigation: challenges and solutions

To estimate divergence, we use the change in size of the ‘hive’ in two consecutive camera frames. To simplify the computations, we neglect perspective effects. Therefore, the ‘hive’ is assumed to have the same square shape from any viewing direction. Then, we get the situation shown in figure 7. Let the number of pixels occupied by the ‘hive’ be Q . With a square shape, this can be converted to the length in pixels

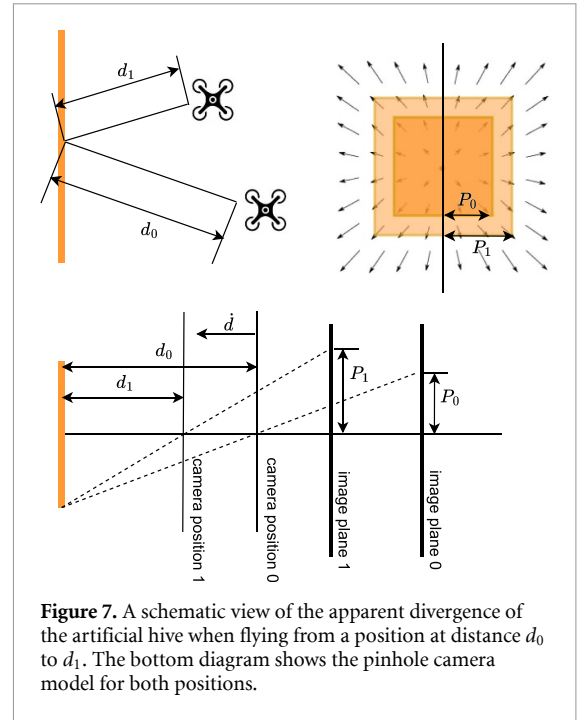


Figure 7. A schematic view of the apparent divergence of the artificial hive when flying from a position at distance d_0 to d_1 . The bottom diagram shows the pinhole camera model for both positions.

with $P = \frac{\sqrt{Q}}{2}$. Assuming the pinhole camera model and defining $v = \dot{d}$, the divergence can be computed with:

$$\lim_{t \rightarrow 0} (\vartheta(t)) = \lim_{t \rightarrow 0} \left(\frac{\dot{d}}{d} \right) = \lim_{t \rightarrow 0} \left(\frac{P_1 - P_0}{\Delta t} \right) \frac{1}{P_0} = \frac{dP}{dt} \frac{1}{P_0}. \quad (10)$$

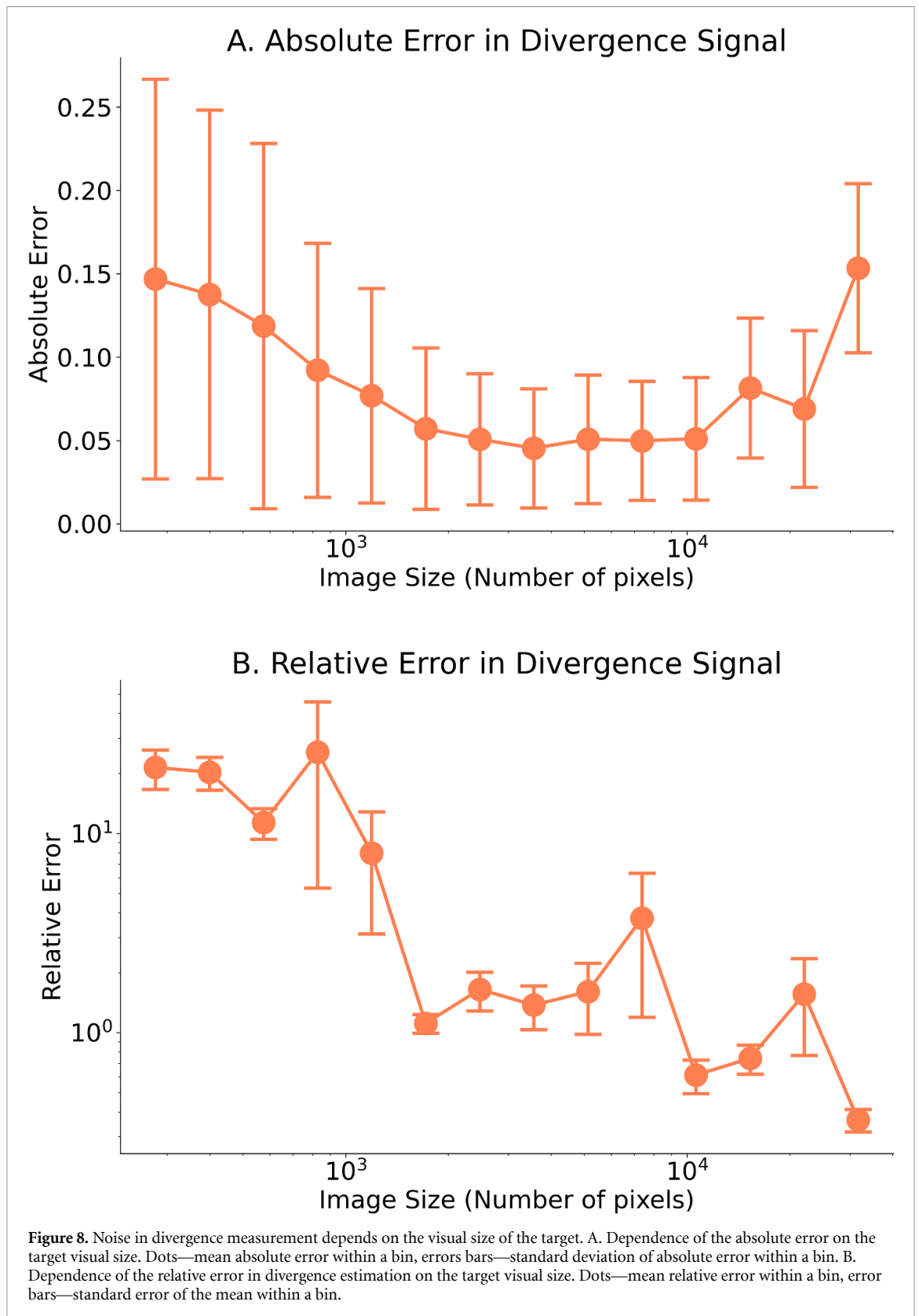
There are three major difficulties in divergence estimation and divergence-based navigation: noise, delays, and oscillations. Below, we discuss each of these problems and describe our solutions to them.

4.1. Noise in divergence estimate depends on the target visual size

The raw divergence estimates contain noise. There are many reasons for this: lens chromatic aberrations, thermal noise in the camera, fluctuations in image acquisition rate, etc. Most importantly, estimation of divergence requires a calculation of derivative, which is an inherently noisy operation as it amplifies high-frequency signal components, which usually are noisy.

Now, the amplitude of the noise is higher when far away from the target. An intuitive reason for this is as follows. When measuring the size of the box, the noise will manifest itself as an error in the pixel count. When far from the box, the box occupies only a few image pixels. Hence, even small errors in the pixel estimates would have a large effect on the divergence measurement. In contrast, when the drone is close to the box, the box occupies a large portion of the image, such that any error in pixel count has a very small effect on the divergence.

To illustrate our point and propose a solution, we performed the following experiment (figure 8). The



drone was approaching the ‘hive’ while being controlled by the OptiTrack system to disentangle drone control behavior from divergence measurements. The drone was following a sine wave modulation of the pitch angle, that provided forward acceleration.

We measured noise in the divergence estimate as an error between the divergence estimate and ground truth. The ground truth divergence was available from the OptiTrack measurements following equation (1). To assess the dependence of absolute

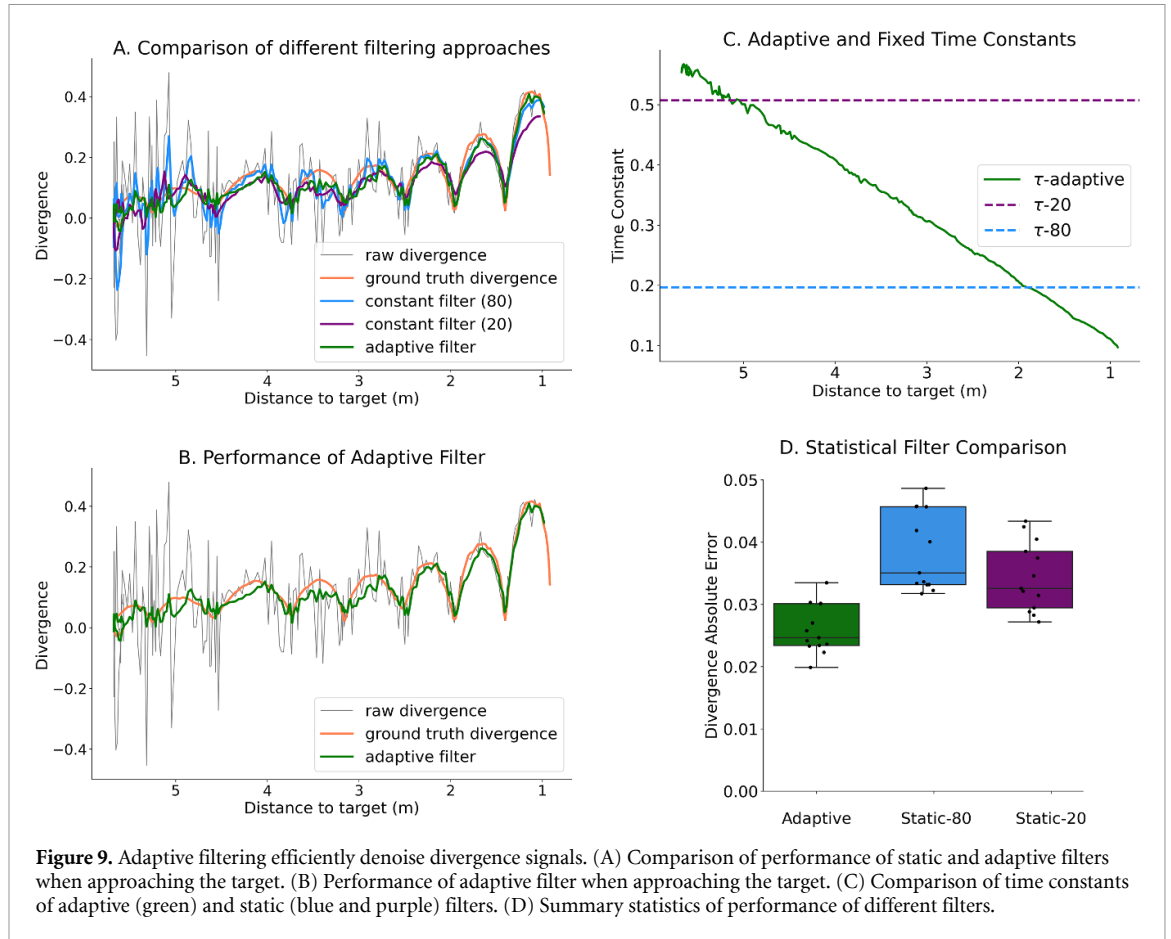


Figure 9. Adaptive filtering efficiently denoise divergence signals. (A) Comparison of performance of static and adaptive filters when approaching the target. (B) Performance of adaptive filter when approaching the target. (C) Comparison of time constants of adaptive (green) and static (blue and purple) filters. (D) Summary statistics of performance of different filters.

error, we binned measured box sizes in logarithmic bins and calculated the mean absolute error (MAE) and its standard deviation for each of the bins (figure 8). As was suggested above, the MAE of the divergence estimate as well as the standard deviation of this error gradually decreases with an increase in the number of pixels.

However, when the ‘hive’ started to occupy most of the camera’s visual field, the absolute error in divergence estimate began to increase again. There are two main factors contributing to it. First of all, our assumptions about system optics (negation of perspective effect, pinhole camera model) become less valid closer to the target, leading to an error in divergence estimate. Secondly, closer to the target we measure larger divergence signals (figure 9). Naturally, it leads to a larger absolute error in the divergence estimate. Yet, plotting relative error in divergence estimate against target visual size (figure 8), one can see that relative error consistently goes down.

The dependence of the noise in divergence estimates was often overlooked in other implementations of the optical-flow-based landings because in majority of studies drone was landing on a large surface [21, 25, 27–34]. As a result, the divergence was calculated from the entire visual field whereas noise in divergence estimates originates from a small target size.

To mitigate noise in the divergence signal, one has to low-pass filter this signal, following the equation (11):

$$\vartheta_{\text{measured}}[t] = \alpha \vartheta_{\text{raw}}[t] + (1 - \alpha) \vartheta_{\text{measured}}[t - 1] \quad (11)$$

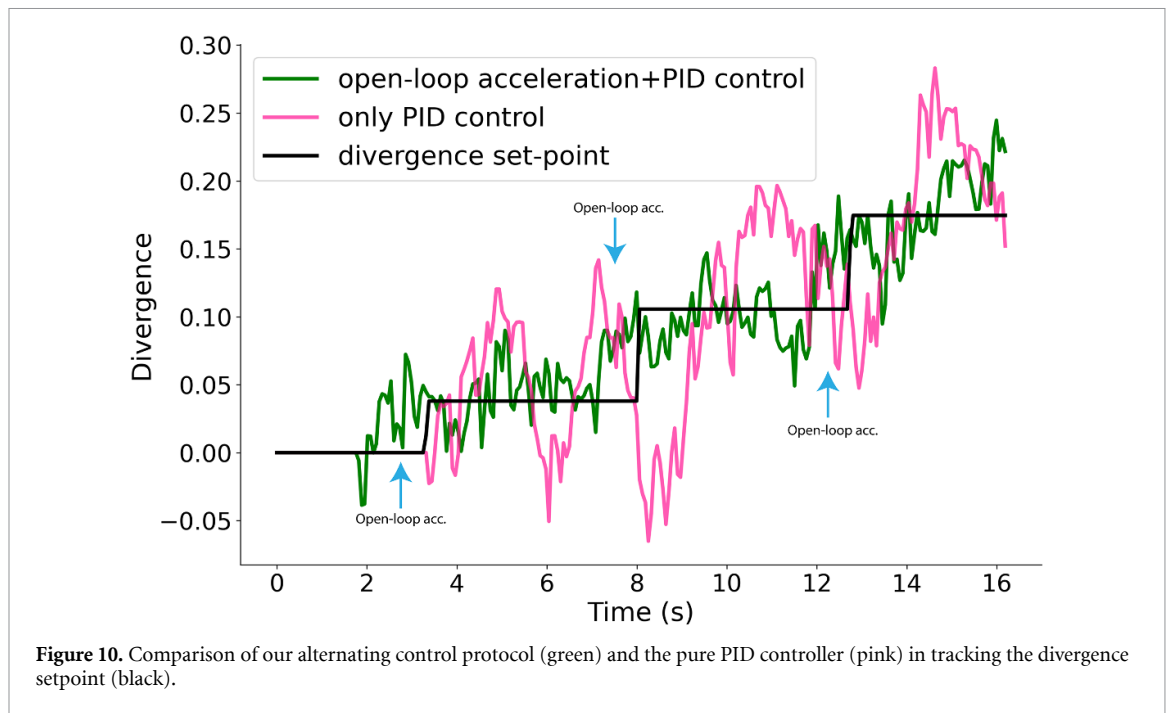
where α is the ratio between the sampling interval dt and the filter time constant τ : $\alpha = \frac{dt}{\tau}$

However, since noise decays upon closing the distance to the target, the requirements for the filter depend on the drone’s position. Far from the target, the noise is high and one needs a low-pass filter with a long time constant. Close to the target, the noise is low and one needs a low-pass filter with a short time constant.

To satisfy both requirements, we propose a low-pass filter with an adaptable time constant that varies with target size following the equation:

$$\tau = \frac{C_{lp}}{\sqrt{Q}} \quad (12)$$

where C_{lp} is a scaling constant. This approach was consistent with the phenomenological models of insect’s visual signal processing [8]. While to the best of our knowledge, there is no direct evidence of insect neurons adapting their time constant specifically to



stimulus size, they do exhibit adaptation to contrast [38]. Contrast adaptation is widely considered to be a fundamental mechanism underlying more complex forms of adaptation and has been shown to drive adaptation to stimulus size in the vertebrate retina [41, 42]. Therefore, we believe the proposed mechanism to be biologically plausible.

To quantify the advantages of an adaptive filter, we performed experiments with the drone approaching the box following the sinewave-modulated pitch law (total 12 flights, with 3 different sinewave frequencies). We then filtered raw divergence through three different filters. Adaptive filter (green trace), whose time constant was gradually changing from ≈ 600 ms to ≈ 100 ms and 2 filters with fixed time constants. One static filter (constant filter 20, purple line) had a long time constant (≈ 500 ms), analogous to the adaptive filter when Q was within the 20th percentile of the color count in a given flight (figure 9(C)). Another static filter (constant filter 80, blue line) had a short time constant (≈ 200 ms), analogous to the adaptive filter when Q was within 80th percentile of the color count in a given flight (figure 9(C)).

In figure 9(A) we plotted raw measured divergence (gray), ground truth divergence (orange), divergence estimated with adaptive filter (green), divergence estimated with constant filter 20 (purple), and divergence estimated with constant filter 80 (blue line). From the plot, it is clear that the blue line contains a lot of noise when the drone is far from the ‘hive’, while the purple line undershoots true divergence when the drone is close to the target. In figure 9(B) we focused on the comparison between adaptive filter and ground truth optical flow divergence. Figure 9(B) shows that the adaptive filter

closely follows ground truth regardless of whether it is far or close to the target. Figure 9(D) makes a quantitative comparison between 3 filter types in terms of absolute error in divergence estimation. In each of the flights, the adaptive filter performed better than filters with static time constant.

4.2. Delays in the divergence estimate

Long delays introduced by the adaptive filter at large distances do not allow good system step-response if change in a divergence set-point is performed by PID controller. This point is illustrated by the pink trace in figure 10. The figure shows that after switch in the divergence set-point, there are decaying oscillations in the divergence signal and poor tracking of the set-point value.

To solve this problem of sluggish sensory integration, we decided to switch between divergence values by applying open-loop input to forward acceleration μ_x and only monitor/control divergence after it settles to a new set-point, with open-loop input yielding reference values for θ and T from equation (6). In figure 11 μ_x is plotted against time. The input is designed to increase ϑ quickly for a short time and then remain constant. ϑ^* is then set to the current ϑ , and the controller is switched back to PID control corresponding with equation (3). Now, the landing is characterized by two repeating phases: an acceleration phase to increase divergence and a deceleration phase to decrease speed while keeping divergence constant, very similar to how it is suggested to be done in insects [6]. This process continues until a target value of ϑ^* is reached. When this happens, the quadrotor keeps decelerating with PID control.

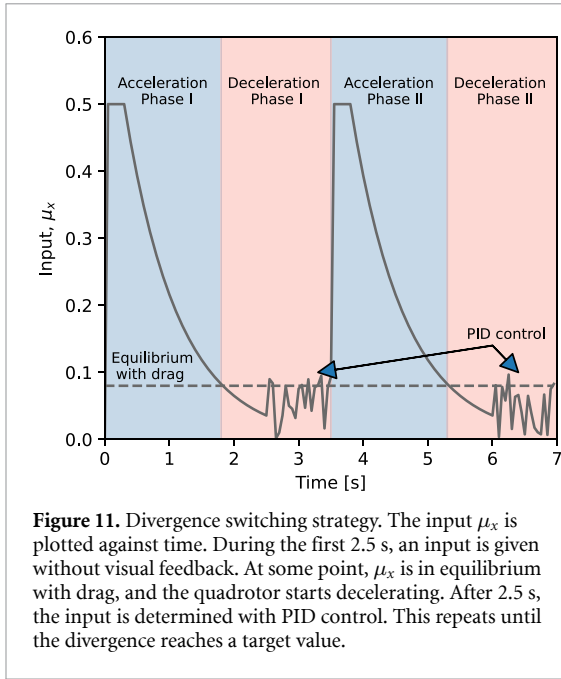


Figure 11. Divergence switching strategy. The input μ_x is plotted against time. During the first 2.5 s, an input is given without visual feedback. At some point, μ_x is in equilibrium with drag, and the quadrotor starts decelerating. After 2.5 s, the input is determined with PID control. This repeats until the divergence reaches a target value.

We experimentally evaluated the improvements in control performance achieved by incorporating an open-loop acceleration command (figure 10). To ensure a controlled comparison—where the only variable was the type of control used—we employed the following protocol. First, we conducted a flight using our proposed controller. Then, we applied recorded setpoint values as control inputs for the PID controller and compared the performance of both controllers in tracking the command.

As shown in figure 10, the PID controller resulted in decaying oscillations in divergence and noticeably poorer setpoint tracking. To quantify this effect, we calculated the MAE between the divergence setpoint and the measured divergence for both control strategies. For the PID controller, the error was computed over the sequence from the moment the measured divergence reached the setpoint until the next setpoint change. For the alternating control strategy, we measured the error between open-loop acceleration command sequences. Our results showed that incorporating open-loop acceleration reduced the MAE by an average of 40% ($n = 7, p = 0.004$, dependent t -test).

4.3. Self-induced oscillations close to target

Previous studies showed that naive optical-flow-based control during landing leads to self-induced oscillations in the final phase of the flight [26, 27], often resulting in a crash. We visualized this problem in figure 12. Figure 12(A) shows that when the distance to the target (pink) becomes less than 2 m, the divergence signal (gray) starts to oscillate around its set-point (black). The oscillation in the divergence signal leads to oscillations in the drone position

(figure 12(B)). As a result, the drone does not land in the box but actually hits the box and gets stuck on top of it. This is evident from the positive, with respect to box position, coordinate of the drone along the Z axis in figure 12(B) (cyan).

These self-induced oscillations originate from a combination of delays in the system and non-linear dependence of the optical flow divergence on distance. When the drone is close to the target, even small changes in distance lead to large changes in divergence. To compensate the system's PID controller (equation (3)) has to decrease the velocity. However, during the sensorimotor delay, the drone moves even closer. As a result, the controller constantly overshoots the desired target leading to oscillations.

To fix it, one needs to decrease P gain in the divergence PID controller (equation (3)) [26, 27]. However, one cannot simply set gain low as the control policy will not be enforced. Hence, one needs to regulate divergence based on the drone's proximity to the target.

We proposed the following approach to this problem. At the end of the acceleration phase, the quadrotor is in equilibrium with the drag force (figure 11). At this equilibrium equation (2) becomes:

$$\begin{bmatrix} 0 \\ 0 \\ g \end{bmatrix} + \frac{1}{m} \begin{bmatrix} \cos \phi \sin \theta \\ -\sin \phi \\ \cos \phi \cos \theta \end{bmatrix} T = \frac{1}{m} \mathbf{F}(\dot{\xi}, w). \quad (13)$$

During the landing, the thrust component in the X_1 direction has the greatest influence on ϑ , especially during the last part of the approach when the quadrotor is centered on the hive. At this point θ is small, $\phi \approx 0$ and $T \approx g$. Then equation (13) can be simplified to:

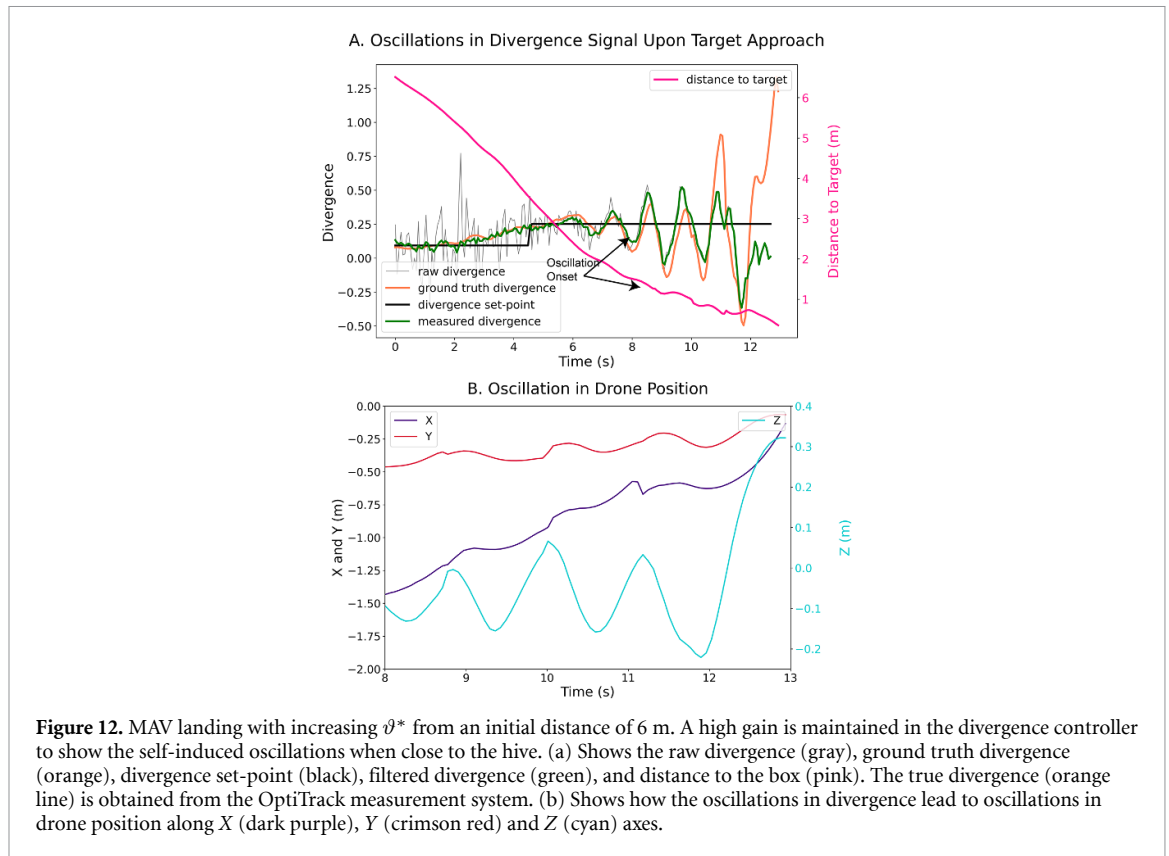
$$\theta g = F_x(\dot{\xi}_x, w_x). \quad (14)$$

The equilibrium velocity is only a function of θ , the drag model, and the wind in the X_1 direction w_x . The initial velocity before the acceleration can be neglected. As the input to θ and the drag model are equal in every acceleration phase, the velocity at the end of the acceleration $\dot{\xi}_{x_e}$ only varies with w_x . Then, from equation (1) we get:

$$\vartheta_e = c_e \frac{\dot{\xi}_{x_e}(w_x)}{\xi_{x_e}} \quad (15)$$

where c_e is a constant that depends on the drag model of the quadrotor that can be determined from flight test data. With this method, ϑ_e is only a function of wind speed and distance to the hive and can, therefore, be used to schedule the control gains in equation (3) as follows:

$$k = \frac{c_e}{\vartheta_e}. \quad (16)$$



5. Visual servoing with switching strategy

To test the actual performance of visual servoing with a switching strategy, we initialized a quadrotor at 18 different starting positions (stars, figure 13). From each position, the drone performed one landing with trajectories plotted in figure 13(A) (top view) and figure 13(B) (side view). Figure 13 shows that in all of the cases the drone was able to land in the box.

Consistent with the autopilot strategy described in section 2.1, in all of the landing trials drone was first dealing with its offset along the Z and Y axes by bringing the ‘hive’ to the center of its visual field (equation (3)) and then approaching the target along X axis. During the flight, the divergence set-point was gradually increased.

We further focused our analysis on the three particular trajectories, denoted with golden stars. For these trajectories, we plotted raw (gray), ground truth (orange), and filtered (green) divergences along divergence setpoint (black) as a function of distance to target (figure 13(C)). In all three cases, raw, measured and ground truth divergences followed the set-points. The pattern of change in divergence following acceleration control is described earlier. Each two-and-a-half-second divergence was increased following the open-loop acceleration before settling on a new set-point value for the next 2.5 s. Upon reaching the threshold size value, the landing procedure was initiated.

At the end of the landing, there was a sharp increase in the difference between ground truth and measured divergence. Two factors contribute to this phenomenon. First of all, closer to the target there is an increase in noise in Optitrack measurements since the box blocks the field of view for some of the Optitrack cameras. Secondly, there is an ambiguity as to what to consider to be the center of the box. When calculating divergence from optic track measurements, we assumed the center of the box to be at the origin of all axes. However, in drone observations, a lot of signal comes from the back wall of the box. Although we are talking here about small differences, around 15–20 cm, they become critical when the box becomes close to the box. Especially, given the hyperbolic dependence between divergence and distance.

6. Conclusions

We implemented bioinspired landing strategy that alternates between decelerations at constant optical flow divergence and accelerations to switch between divergence set-points for visual servoing onboard a quadrotor (figure 1). Compared to the ‘constant’ divergence strategy, where the agent decelerates with a single divergence setpoint, the ‘switching’ strategy offers clear benefits. It allows the agent to adapt its steering based on visual input. Two cases are instructive (figure 6): first, switching increases speed, enabling faster landings with higher average speed

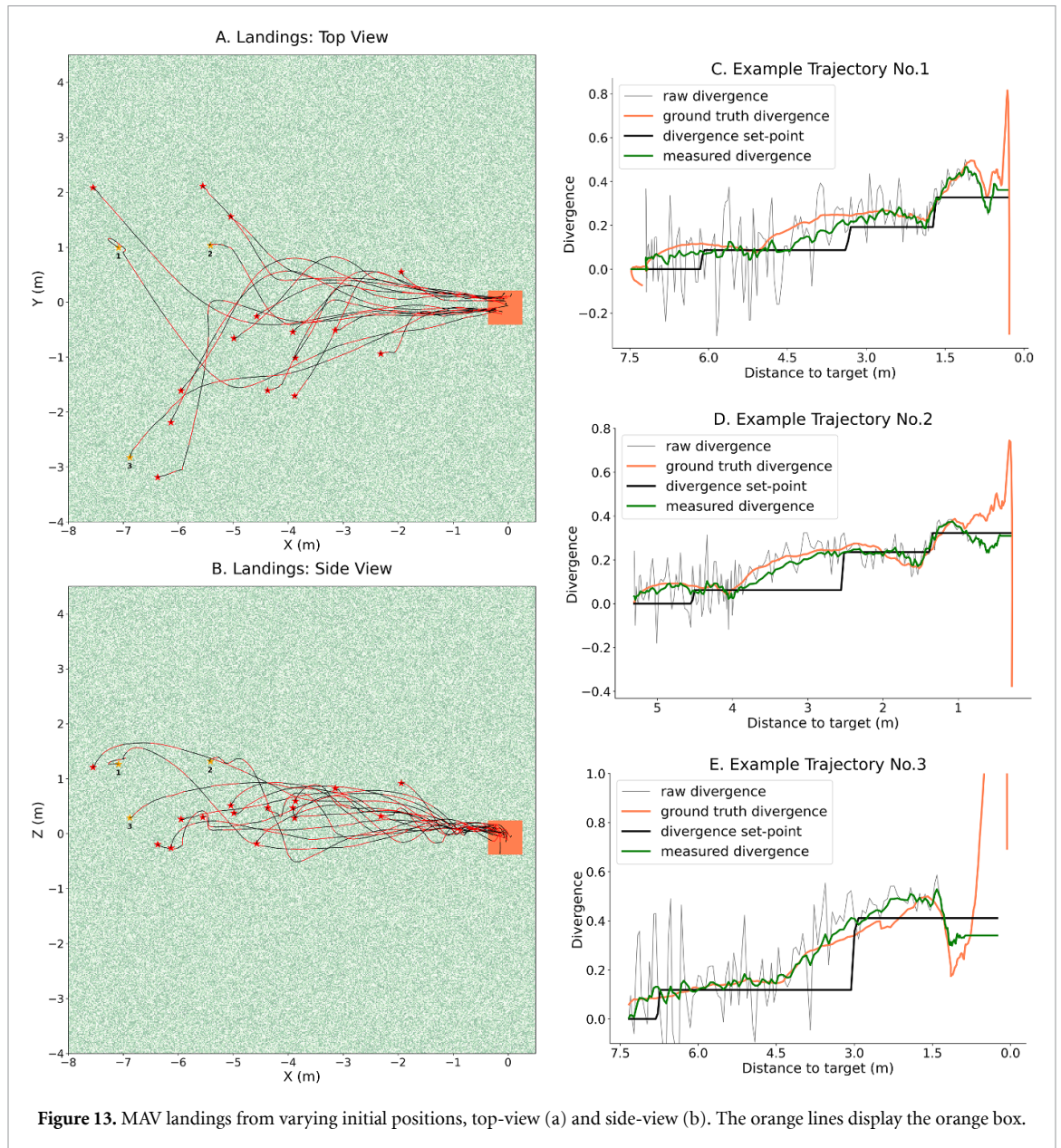


Figure 13. MAV landings from varying initial positions, top-view (a) and side-view (b). The orange lines display the orange box.

(figure 6(A)); second, it allows faster landings while maintaining lower maximum speed, which is crucial for safety in cluttered environments with higher collision risks.

In particular, the issues encountered during the implementation of the switching strategy (figures 8–12) stem from fundamental limitations of visual signals. While oscillations in divergence signal and drone position near the landing surface (figure 12) have been previously discussed in the literature [26, 27], we identified two additional challenges. First, the divergence signal from a landing surface is significantly corrupted by noise when target has a small visual size (figure 8). To improve SNR the divergence signal must be filtered using a low-pass filter with a slow time constant (≈ 500 ms), figure 9). However, this filtering introduces a secondary issue: it causes decaying oscillations and sluggish step-response in

divergence signal when the switching in set-point is done with PID controller (figure to address this, we employed open-loop forward acceleration as a method of divergence switching 10. Here, our method complements an influential theory of sensorimotor convergence [19, 43]. While this theory suggests that sensory processing is shaped to align with an agent’s actuation capabilities, our approach selects control commands to compensate for the limitations of the sensory system.

Although our study considers a simplified case of visual servoing compared to real-world tasks [44–47], we believe our findings are relevant to broader robotics applications beyond serving as a ‘model organism’ for studying biological theories. Vision-based navigation is a valuable tool that can augment or even replace other navigational sensors in scenarios where their signals are unavailable—such as GPS, which

performs poorly indoors or near buildings—or when payload constraints limit sensor selection [44–46, 48]. Consequently, bioinspired methods for optical flow sensing [49–53] and vision-guided navigation [11, 46, 54–59] play a crucial role in modern robotics research, with numerous studies dedicated to landing using constant divergence [21, 25, 27–34, 60, 61]. Our results suggest that a switching divergence strategy can improve landing performance.

Data availability statement

The data that support the findings of this study are openly available at the following URL/DOI: <https://github.com/tudelft/SwitchDivServ>.

Acknowledgments

This work was supported by the Sony Research Award Program awarded to Prof. Guido C H E de Croon, Grant from Air Force Office of Scientific Research (Award Number FA8655-24-1-7061) awarded to Prof. Guido C H E de Croon, and NWO Vidi Grant (VI.Vidi.193.054) awarded to Prof. Florian T Muijres.

Appendix A

Here we will demonstrate that, in the case of equal divergence averaged over the flown distance, the switching strategy leads to a faster landing, given a sufficient flown distance.

In the constant strategy, we have divergence ϑ_0 and flown distance d_0 , measured in meters. Since with exponential decay, 0 is never strictly reached, we assume that landing occurs when the distance to the target is 0.1 m.

In the switching strategy, the total flown distance is the same, d_0 , and the divergence is switched from ϑ_1 to ϑ_2 :

$$\vartheta_2 = \alpha\vartheta_1, \quad (17)$$

at an arbitrary point where the remaining flying distance is d_2 :

$$d_2 = \gamma d_0. \quad (18)$$

Then at the moment of the switch, the drone covered distance d_1 :

$$d_1 = (1 - \gamma) d_0. \quad (19)$$

Since we posit equal divergence averaged over-flown distance, one can express ϑ_0 as a function of ϑ_1 :

$$\vartheta_0 = \vartheta_1(1 - \gamma) + \alpha\gamma\vartheta_1, \quad (20)$$

or:

$$\vartheta_0 = \vartheta_1(1 - \gamma + \alpha\gamma). \quad (21)$$

Now, the time that it would take for a constant divergence strategy to reach 0.1 m from the target can be found in this equation:

$$0.1 = d_0 e^{-\vartheta_0 t_0}, \quad (22)$$

as:

$$t_0 = \frac{\ln(10d_0)}{\vartheta_1(1 - \gamma + \alpha\gamma)}. \quad (23)$$

For the switching strategy, this time would be the sum of t_1 and t_2 . t_1 can be calculated from the equation:

$$\gamma d_0 = d_0 e^{-\vartheta_1 t_1}, \quad (24)$$

as:

$$t_1 = \frac{-\ln(\gamma)}{\vartheta_1}. \quad (25)$$

Similarly, for t_2 :

$$0.1 = \gamma d_0 e^{-\vartheta_2 t_2}, \quad (26)$$

$$t_2 = \frac{\ln(10d_0\gamma)}{\alpha\vartheta_1}. \quad (27)$$

Effectively, we want to prove that:

$$-\frac{\ln(\gamma)}{\vartheta_1} + \frac{\ln(10d_0\gamma)}{\alpha\vartheta_1} < \frac{\ln(10d_0)}{\vartheta_1(1 - \gamma + \alpha\gamma)} \quad (28)$$

$$\frac{\ln(10d_0) - \alpha\ln(\gamma) + \ln(\gamma)}{\alpha} < \frac{\ln(10d_0)}{(1 - \gamma + \alpha\gamma)}. \quad (29)$$

Now, let us bring equations to the common denominator and bring all elements with d_0 to one side of the inequality. We will end up with the following formula:

$$(1 - \alpha)(1 - \gamma + \alpha\gamma)\ln(\gamma) < (\alpha - 1 + \gamma - \gamma\alpha)\ln(10d_0). \quad (30)$$

The resulting inequality can be re-written as:

$$-1(\alpha - 1)(1 - \gamma + \alpha\gamma)\ln(\gamma) < (\alpha - 1)(1 - \gamma)\ln(10d_0). \quad (31)$$

Now, since $\alpha > 1$, we can divide both sides by $(\alpha - 1)$. Keeping in mind that since $\gamma < 1$, its logarithm is negative, we can arrive at the following inequality:

$$(1 - \gamma + \alpha\gamma)|\ln(\gamma)| < (1 - \gamma)\ln(10d_0). \quad (32)$$

Thus, given sufficient flown distance d_0 , that can be calculated for each α and γ switching strategy will always lead to faster landing while requiring smaller maximal velocity. Therefore, with this strategy, one can get both faster and safer landings.

ORCID iDs

Sander T Hazelaar  <https://orcid.org/0009-0006-4030-6276>

Chenyao Wang  <https://orcid.org/0009-0001-1493-5355>

Christophe de Wagter  <https://orcid.org/0000-0002-6795-8454>

Florian T Muijres  <https://orcid.org/0000-0002-5668-0653>

Guido C H E de Croon  <https://orcid.org/0000-0001-8265-1496>

Matthew Yedutenko  <https://orcid.org/0000-0003-3896-8984>

References

- [1] Heinrich B 1979 Resource heterogeneity and patterns of movement in foraging bumblebees *Oecologia* **40** 235–45
- [2] Wagner H 1982 Flow-field variables trigger landing in flies *Nature* **297** 147–8
- [3] Baird E, Boeddeker N, Ibbotson M R and Srinivasan M V 2013 A universal strategy for visually guided landing *Proc. Natl Acad. Sci.* **110** 18686–91
- [4] van Breugel F and Dickinson M 2012 The visual control of landing and obstacle avoidance in the fruit fly *Drosophila melanogaster* *J. Exp. Biol.* **215** 1783–98
- [5] Goyal P, Cribellier A, De Croon G C H E, Lankheet M J, van Leeuwen J L, Pieters R P M and Muijres F T 2021 Bumblebees land rapidly and robustly using a sophisticated modular flight control strategy *iScience* **24** 102407
- [6] Goyal P, van Leeuwen J L and Muijres F T 2022 Bumblebees land rapidly by intermittently accelerating and decelerating toward the surface during visually guided landings *iScience* **25** 104265
- [7] Goyal P, Baird E, Srinivasan M V and Muijres F T 2023 Visual guidance of honeybees approaching a vertical landing surface *J. Exp. Biol.* **226** jeb245956
- [8] Borst A, Haag J and Reiff D F 2010 Fly motion vision *Annu. Rev. Neurosci.* **33** 49–70
- [9] Borst A 2014 Fly visual course control: behaviour, algorithms and circuits *Nat. Rev. Neurosci.* **15** 590–9
- [10] Chang J J, Crall J D and Combes S A 2016 Wind alters landing dynamics in bumblebees *J. Exp. Biol.* **219** 2819–22
- [11] de Croon G C H E, Dupeyroux J J G, Fuller S B and Marshall J A R 2022 Insect-inspired AI for autonomous robots *Sci. Robot.* **7** eabl6334
- [12] Ijspeert A J 2014 Biorobotics: using robots to emulate and investigate agile locomotion *Science* **346** 196–203
- [13] Jonas E and Paul Kording K 2017 Could a neuroscientist understand a microprocessor? *PLOS Comput. Biol.* **13** 1–24
- [14] de Croon G C H E, Dupeyroux J J G, De Wagter C, Chatterjee A, Olejnik D A and Ruffier F 2022 Accommodating unobservability to control flight attitude with optical flow *Nature* **610** 485–90
- [15] Karásek M, Muijres F T, De Wagter C, Remes B D W and de Croon G C H E 2018 A tailless aerial robotic flapper reveals that flies use torque coupling in rapid banked turns *Science* **361** 1089–94
- [16] Franceschini N, Ruffier F and Serres J 2007 A bio-inspired flying robot sheds light on insect piloting abilities *Curr. Biol.* **17** 329–35
- [17] Wilshin S, Amos S and Bomphrey R J 2023 Seeing with sound; surface detection and avoidance by sensing self-generated noise *Int. J. Micro Air Vehicles* **15** 17568293221148377
- [18] Zhu H, Bordner K, Bomphrey R J, Usherwood J R, Haughn K and Harvey C 2025 *Distributed Pressure Sensing for Analyzing Aerodynamic Characteristics in Avian-Like Formation Flight, Chapter Session: Bio-Inspired Adaptive Structures* (AIAA) p 1460
- [19] Turin Z, Taylor G K, Krapp H G, Jensen E and Sean Humbert J 2025 Matching sensing to actuation and dynamics in distributed sensorimotor architectures *IEEE Access* **13** 13584–605
- [20] Biewener A A, Bomphrey R J, Daley M A and Ijspeert A J 2022 Stability and manoeuvrability in animal movement: lessons from biology, modelling and robotics *Proc. R. Soc. B* **289** 20212492
- [21] Van Breugel F, Morgansen K and Dickinson M H 2014 Monocular distance estimation from optic flow during active landing maneuvers *Bioinspir. Biomim.* **9** 025002
- [22] Ma K Y, Chirarattananon P, Fuller S B and Wood R J 2013 Controlled flight of a biologically inspired, insect-scale robot *Science* **340** 603–7
- [23] Clawson T S, Ferrari S, Fuller S B and Wood R J 2016 Spiking neural network (SNN) control of a flapping insect-scale robot 2016 *IEEE 55th Conf. on Decision and Control (CDC)* pp 3381–8
- [24] Plett J, Bahl A, Buss M, Kühnlenz K and Borst A 2012 Bio-inspired visual ego-rotation sensor for MAVs *Biol. Cybern.* **106** 51–63
- [25] Serres J R and Ruffier F 2017 Optic flow-based collision-free strategies: from insects to robots *Arthropod Struct. Dev.* **46** 703–17
- [26] de Croon G C H E 2016 Monocular distance estimation with optical flow maneuvers and efference copies: a stability-based strategy *Bioinspir. Biomim.* **11** 016004
- [27] De Croon G C H E, De Wagter C and Seidl T 2021 Enhancing optical-flow-based control by learning visual appearance cues for flying robots *Nat. Mach. Intell.* **3** 33–41
- [28] Herisse B, Hamel T, Mahony R and Russotto F-X 2010 The landing problem of a VTOL Unmanned Aerial Vehicle on a moving platform using optical flow 2010 *IEEE/RJSJ Int. Conf. on Intelligent Robots and Systems* pp 1600–5
- [29] Herissé B, Hamel T, Mahony R and Russotto F 2012 Landing a VTOL unmanned aerial vehicle on a moving platform using optical flow *IEEE Trans. Robot.* **28** 77–89
- [30] Ruffier F and Franceschini N 2004 Visually guided micro-aerial vehicle: automatic take off, terrain following, landing and wind reaction 2004. *IEEE Int. Conf. on Robotics and Automation, 2004. Proc. ICRA'04, 2004* vol 3 pp 2339–46
- [31] Ho H W, De Croon G C H E, van Kampen E, Chu Q P and Mulder M 2018 Adaptive gain control strategy for constant optical flow divergence landing *IEEE Trans. Robot.* **34** 508–16
- [32] Hagenaaers J, Paredes-Vallés F, Bohté S M and de Croon G C H E 2020 Evolved neuromorphic control for high speed divergence-based landings of MAVs *CoRR* (arXiv:2003.03118)
- [33] Pijnacker Hordijk B J, Scheper K Y W and de Croon G C H E 2017 Vertical landing for micro air vehicles using event-based optical flow *J. Field Robot.* **35** 69–90
- [34] Scheper K Y W and de Croon G C H E 2020 Evolution of robust high speed optical-flow-based landing for autonomous MAVs *Robot. Auton. Syst.* **124** 103380
- [35] Corke P and Good M C 1992 Dynamic effects in high-performance visual servoing *Proc. 1992 IEEE Int. Conf. on Robotics and Automation* pp 1838–43
- [36] Mahony R, Corke P and Hamel T 2007 Dynamic image-based visual servo control using centroid and optic flow features *J. Dyn. Syst. Meas. Control* **130** 12
- [37] Serra P, Cunha R, Hamel T, Cabecinhas D and Silvestre C 2016 Landing of a quadrotor on a moving target using

- dynamic image-based visual servo control *IEEE Trans. Robot.* **32** 1524–35
- [38] Fairhall A L, Lewen G D, Bialek W and de Ruyter van Steveninck R R 2001 Efficiency and ambiguity in an adaptive neural code *Nature* **412** 787–92
- [39] Dyer A G, Neumeyer C and Chittka L 2005 Honeybee (*Apis mellifera*) vision can discriminate between and recognise images of human faces *J. Exp. Biol.* **208** 4709–14
- [40] Smeur E J J, Chu Q P and de Croon G C H E 2015 Adaptive incremental nonlinear dynamic inversion for attitude control of micro air vehicles *J. Guid. Control Dyn.* **39** 450–61
- [41] Smirnakis S M, Berry M J, Warland D K, Bialek W and Meister M 1997 Adaptation of retinal processing to image contrast and spatial scale *Nature* **386** 69–73
- [42] Yedutenko M, Howlett M H C and Kamermans M 2021 High contrast allows the retina to compute more than just contrast *Front. Cell. Neurosci.* **14** 595193
- [43] Taylor G K and Krapp H G 2007 Sensory systems and flight stability: what do insects measure and why? *Insect Mechanics and Control (Advances in Insect Physiology vol 34)* ed J Casas and S J Simpson (Academic) pp 231–316
- [44] De Silva S C, Phlernjai M, Rianmora S and Ratsamee P 2022 Inverted docking station: a conceptual design for a battery-swapping platform for quadrotor UAVs *Drones* **6** 56
- [45] Schäfer B E, Picchi D, Engelhardt T and Abel D 2016 Multicopter unmanned aerial vehicle for automated inspection of wind turbines 2016 24th Mediterranean Conf. on Control and Automation (MED) pp 244–9
- [46] Floreano D and Wood R J 2015 Science, technology and the future of small autonomous drones *Nature* **521** 460–6
- [47] Machkour Z, Ortiz-Arroyo D and Durdevic P 2021 Classical and deep learning based visual servoing systems: a survey on state of the art *J. Intell. Robot. Syst.* **104** 11
- [48] Kumar V and Michael N 2012 Opportunities and challenges with autonomous micro aerial vehicles *Int. J. Robot. Res.* **31** 1279–91
- [49] Gallego G et al 2022 Event-based vision: a survey *IEEE Trans. Pattern Anal. Mach. Intell.* **44** 154–80
- [50] Milde M B, Bertrand O J N, Ramachandran H, Egelhaaf M and Chicca E 2018 Spiking elementary motion detector in neuromorphic systems *Neural Comput.* **30** 2384–417
- [51] Yedutenko M, Paredes-Valles F, Khacef L and De Croon G C H E 2024 TDE-3: an improved prior for optical flow computation in spiking neural networks (arXiv:2402.11662)
- [52] Shen C, Zhao X, Wu X, Cao H, Wang C, Tang J and Liu J 2024 Multiaperture visual velocity measurement method based on biomimetic compound-eye for UAVs *IEEE Internet Things J.* **11** 11165–74
- [53] Shen C, Xiong Y, Zhao D, Wang C, Cao H, Song X, Tang J and Liu J 2022 Multi-rate strong tracking square-root cubature Kalman filter for MEMS-INS/GPS/polarization compass integrated navigation system *Mech. Syst. Signal Process.* **163** 108146
- [54] Sanket N, Singh C, Ganguly K, Fermüller C and Aloimonos Y 2018 GapFly: active vision based minimalist structure-less gap detection for quadrotor flight (IEEE) (<https://doi.org/10.1109/LRA.2018.2843445>)
- [55] Shen C, Wu Y, Qian G, Wu X, Cao H, Wang C, Tang J and Liu J 2025 Intelligent bionic polarization orientation method using biological neuron model for harsh conditions *IEEE Trans. Pattern Anal. Mach. Intell.* **47** 789–806
- [56] Liu X, Tang J, Shen C, Wang C, Zhao D, Guo X, Li J and Liu J 2023 Brain-like position measurement method based on improved optical flow algorithm *ISA Trans.* **143** 221–30
- [57] Firliefyn M V M, Hagenars J J and De Croon G C H E 2024 Direct learning of home vector direction for insect-inspired robot navigation 2024 *IEEE Int. Conf. on Robotics and Automation (ICRA)* pp 6022–8
- [58] van Dijk T, De Wagter C and de Croon G C H E 2024 Visual route following for tiny autonomous robots *Sci. Robot.* **9** eadk0310
- [59] Schoepe T, Janotte E, Milde M B, Bertrand O J N, Egelhaaf M and Chicca E 2024 Finding the gap: neuromorphic motion-vision in dense environments *Nat. Commun.* **15** 817
- [60] Dupeyroux J, Hagenars J J, Paredes-Vallés F and de Croon G C H E 2021 Neuromorphic control for optic-flow-based landing of MAVs using the Loihi processor 2021 *IEEE Int. Conf. on Robotics and Automation (ICRA)* pp 96–102
- [61] Paredes-Vallés F, Hagenars J J, Dupeyroux J, Stroobants S, Xu Y and de Croon G C H E 2024 Fully neuromorphic vision and control for autonomous drone flight *Sci. Robot.* **9** eadi0591